

Protostellar disk accretion in turbulent filaments

S. Heigl^{1,2}, E. Hoemann^{2,3}, and A. Burkert^{1,2,3}

¹ Universitäts-Sternwarte, Ludwig-Maximilians-Universität München, Scheinerstr. 1, 81679 Munich, Germany
e-mail: heigl@usm.lmu.de

² Excellence Cluster ORIGINS, Boltzmannstrasse 2, 85748 Garching, Germany

³ Max-Planck Institute for Extraterrestrial Physics, Giessenbachstr. 1, 85748 Garching, Germany

Received; accepted

ABSTRACT

Context. Recent observations of protostellar cores suggest that most of the material in the protostellar phase is accreted along streamers. Streamers in this context are defined as velocity coherent funnels of denser material potentially connecting the large scale environment to the small scales of the forming accretion disk.

Aims. Using simulations which simultaneously resolve the driving of turbulence on the filament scale as well as the collapse of the core down to protostellar disk scales, we aim to understand the effect of the turbulent velocity field on the formation of overdensities in the accretion flow.

Methods. We perform a three-dimensional numerical study on a core collapse within a turbulent filament using the RAMSES code and analyse the properties of overdensities in the accretion flow.

Results. We find that overdensities are formed naturally by the initial turbulent velocity field inherited from the filament and subsequent gravitational collimation. This leads to streams which are not really filamentary but show a sheet-like morphology. Moreover, they have the same radial infall velocities as the low density material. As a main consequence of the turbulent initial condition, the mass accretion onto the disk does not follow the predictions for solid body rotation. Instead, most of the mass is funneled by the overdensities to intermediate disk radii.

Key words. stars:formation – stars:protostars – ISM:kinematics and dynamics – ISM:structure

1. Introduction

While the classical picture of star formation assumes the gravitational collapse of an isolated spherical stellar core similar to a Bonnor-Ebert or singular isothermal sphere (Larson 1969; Penston 1969; Shu 1977; Foster & Chevalier 1993), it is now well supported that most star forming cores lie within filaments of molecular clouds (André et al. 2014). Consequently, stars do not form in isolation but can accrete actively from their environment. This picture also has been established by observations with the emergence of streamers, velocity coherent non-isotropic accretion structures, which have been detected during all stages in the evolution of young stellar objects (Pineda et al. 2023).

During the disk build-up in embedded protostellar class-0/I objects, non-isotropic accretion streams have been observed in dust (Le Gouellec et al. 2019) and molecular emission (Cabedo et al. 2021; Murillo et al. 2022; Valdivia-Mena et al. 2022; Kido et al. 2023). Typically, the measured sizes are around a few thousand AU with accretion rates of around $1.0 \times 10^{-6} M_{\odot} \text{ yr}^{-1}$. However, there have been cases of streamers extending up to 10000 AU (Pineda et al. 2020) and accretion rates exceeding $1.0 \times 10^{-5} M_{\odot} \text{ yr}^{-1}$ (Valdivia-Mena et al. 2023). Most observations show an one major accretion stream onto a single core. Nonetheless, there have been detections of more complex structures such as multiple streamers (Thieme et al. 2022) and streamers accreting onto binary system (Hsieh et al. 2023).

Non-isotropic infall has a major impact on the forming protoplanetary disk, potentially leading to various substructures and instabilities (Bae et al. 2015; Lesur et al. 2015; Kuffmeier et al. 2021; Kuznetsova et al. 2022). This raises the fundamental ques-

tion if planet formation already begins during the build-up of the disk in the class-0 phase in contrast to an isolated unperturbed disk in the class-II phase which is often assumed (Testi et al. 2014; Lesur et al. 2022). Not only was it shown by Drażkowska & Dullemond (2018) that planetesimals may form during infall, but there is even growing observational evidence that planet formation may start at an earlier stage. Submillimeter observations of disks in the class-II phase show insufficient dust masses to explain the formation of exoplanetary systems (Najita & Kenyon 2014; Ansdell et al. 2017; Manara et al. 2018) in contrast to dust masses of disks in the class-0/I phase (Greaves & Rice 2011; Tychoniec et al. 2018; Tobin et al. 2020; Tychoniec et al. 2020). Additionally, there are indications of dust growth in the early phases of disk formation (Kwon et al. 2009; Harsono et al. 2018; Hsieh et al. 2019; Segura-Cox et al. 2020). Finally, the isotopic distribution in meteorites (Kruijjer et al. 2014; Van Kooten et al. 2016; Kruijjer et al. 2017) and lack of water in the inner Solar System (Morbidelli et al. 2016) suggest the early formation of a dynamical barrier such as Jupiter.

Several numerical studies have also shown that the large scales play an essential role for the distribution of mass accretion onto the disk. Models of collapsing cores including turbulence and magnetic fields usually lead to the formation of accretion channels onto the disk (Walch et al. 2010; Joos et al. 2013; Seifried et al. 2013, 2015; Matsumoto et al. 2017; Lam et al. 2019; Hennebelle et al. 2020). These can have a major impact on the accretion source function which specifies where accreted material enters the disk. For example, Lee et al. (2021) detected larger accretion rates towards the centre than expected from angular momentum conservation of solid body rotation.

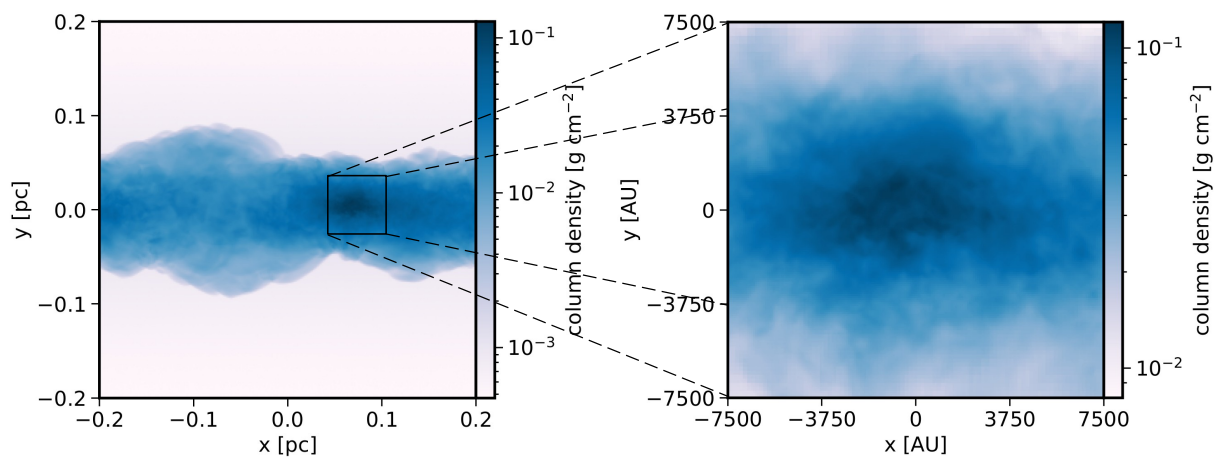


Fig. 1: Projection of the core at 93.2 kyr before its collapse and sink particle creation. The left hand side shows the projection of the whole box with a size of 0.4 pc. The right hand side shows a zoom onto the core with a radius of 7500 AU. One can see that the core shows substructure as it inherits turbulent motions from the large scale filament.

Some studies were also able to self-consistently resolve the dynamical range from molecular clouds down to the disk using either adaptive mesh refinement (Kuffmeier et al. 2017, 2018, 2019; Lebreuilly et al. 2021; Pelkonen et al. 2021; Kuffmeier et al. 2023) or SPH methods (Bate 2018). Despite the different set-ups and physics used, all of the simulations stress that the inhomogeneous accretion via streamers is highly dependent on the environment and leads to instabilities, disk misalignment and even late replenishment of the disk (Kuffmeier et al. 2023).

While star formation can take place in molecular clouds in various different environments, the purpose of this paper is to explore the case of a collapsing core within a turbulent filament. The turbulent environment of the core is generated self-consistently by gas accretion onto the filament. As we do not resolve the full physics needed to explore the disk evolution, we concentrate on the analysis of the accretion onto the disk itself. The paper is organised as follows: first we present the numerical simulation and initial condition in section 2. Thereafter, we present the results in section 3 and its various subsections. We compare our simulation to other numerical studies in section 4 and conclude in section 5.

2. Numerical set-up

The simulation was run with the code `RAMSES` by Teyssier (2002) using the MUSCL scheme (Monotonic Upstream-Centred Scheme for Conservation Laws, van Leer 1977), a second-order Godunov scheme for solving the discretised Euler equations in conservative form on a Cartesian grid. As Riemann solver we used the HLLC-Solver (Harten-Lax-van Leer-Contact, Toro et al. 1994) together with the multidimensional MC slope limiter (monotonized central-difference, van Leer 1979).

We set up a forming filament in a radially converging flow as defined in Heigl et al. (2020) as an large-scale initial condition. The simulation consists of an isothermal 3D box of size 0.1 pc with periodic boundary conditions in the filament direction, in this case the x -axis. The isothermal temperature is set to 10.0 K and a molecular weight of $\mu = 2.36$ which results in a sound speed of around 0.19 km s^{-1} . We define a cylindrical inflow in a cylindrical shell at the edge of the box onto the central x -axis with a fixed density and radial velocity which are constantly reset at every time-step. In order to break the symmetry the density

in the inflow region is varied on a cell-by-cell basis with a random value which varies around the mean with a maximum of 50%. The inflow density and the density inside the domain is set to $3.92 \times 10^{-22} \text{ g cm}^{-3}$ which corresponds to a particle density of about $1.0 \times 10^2 \text{ cm}^{-3}$ and the inflow velocity is set to Mach 6.0 for the isothermal gas which equals a velocity of 1.13 km s^{-1} . The mass accretion rate per length onto the filament therefore corresponds to $\dot{M}/L = 8.4 M_{\odot} \text{ pc}^{-1} \text{ Myr}^{-1}$. This flow not only acts as an external pressure to confine the filament material but also drives turbulence inside the filament which quickly settles to a constant level. As shown in Heigl et al. (2018), the turbulence velocity is around 0.23 km s^{-1} , or Mach 1.18, for an inflow velocity of Mach 6.0. This value is independent of the accretion flow density itself as well as the strength of its random variation as kinetic energy is converted to turbulent energy. However, the turbulent velocity does show an anti-correlation to the density profile with the centre of the filament showing lower values than the surface.

The minimum resolution of the simulation is 256^3 cells which is equivalent to $1.56 \times 10^{-3} \text{ pc}$ or about 323 AU. However, we heavily make use of adaptive mesh refinement in order to resolve the scales down to the creation of an accretion disk with a maximum resolution of 16383^3 cells corresponding to $2.44 \times 10^{-5} \text{ pc}$ or 5.04 AU. In order to minimise dissipation across refinement levels and to resolve thin streamer structures in a large region around the forming disk, we employ an aggressive refinement criterion where the Truelove criterion for the maximum density has to be fulfilled by a factor of 128 (Truelove et al. 1997).

As soon as the maximum refinement level reaches a density of $1.83 \times 10^{-13} \text{ g cm}^{-3}$ where the Jean's length is not resolved by at least four cells, a sink particle is placed in the centre if the region fulfills several conditions. In the standard version of `RAMSES` these conditions consist mainly of the gravitational potential dominating over the thermal and kinetic support. We also allow mass accretion onto the sinks by using the implemented Bondi accretion algorithm with the standard setting of the accretion radius of four cells. The amount and distribution of sink particles strongly depend on the formation conditions and the subsequent accretion. However, as this paper's main focus is the creation of streamers and as we do not include enough physics to properly describe the processes inside of the disk, we will explore the sink population in a future paper. In this study, the main purpose of

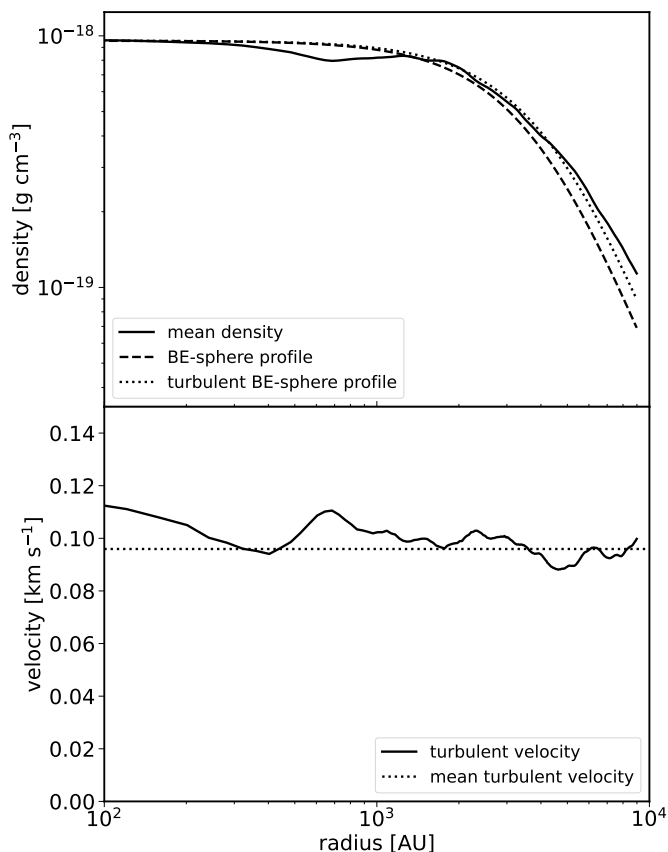


Fig. 2: Radial density and velocity profiles of the forming core 93.2 kyr before its collapse. The upper panel shows the mean density profile as solid black line together with Bonner-Ebert sphere profiles where the dashed line is an isothermal model and the dotted line has an additional turbulent term. For this, we use the turbulent velocity and its mean given in the lower panel as solid and dotted black lines.

the sink particles is to take the role of a mass sink in order to keep the simulation running. Doing so, their impact on the streamers are minimal.

3. Results

3.1. Core collapse and disk formation

Over time a turbulent filament forms inside the box constrained by the accretion pressure of the radial flow. As soon as the filament's line-mass reaches close to critical values given by

$$\left(\frac{M}{L}\right)_{\text{crit}} = \frac{2c_s^2}{G} \approx 1.06 \times 10^{16} \text{ g cm}^{-1} \approx 16.4 M_{\odot} \text{ pc}^{-1}, \quad (1)$$

with c_s being the isothermal sound speed and G being the gravitational constant, a core begins to form as shown in Figure 1. We do not impose any overdensity in the initial condition or the accretion flow and the location where the core forms is only determined by the initial seed for the random number generator. The core itself shows turbulent motions and substructure. Before its collapse, the core's density profile closely follows a Bonnor-Ebert distribution as shown in the upper panel of Figure 2. The measured mean density in each radial bin is given by the solid line together with its standard deviation shown as the gray area. We compare it to the isothermal Bonnor-Ebert profile shown as

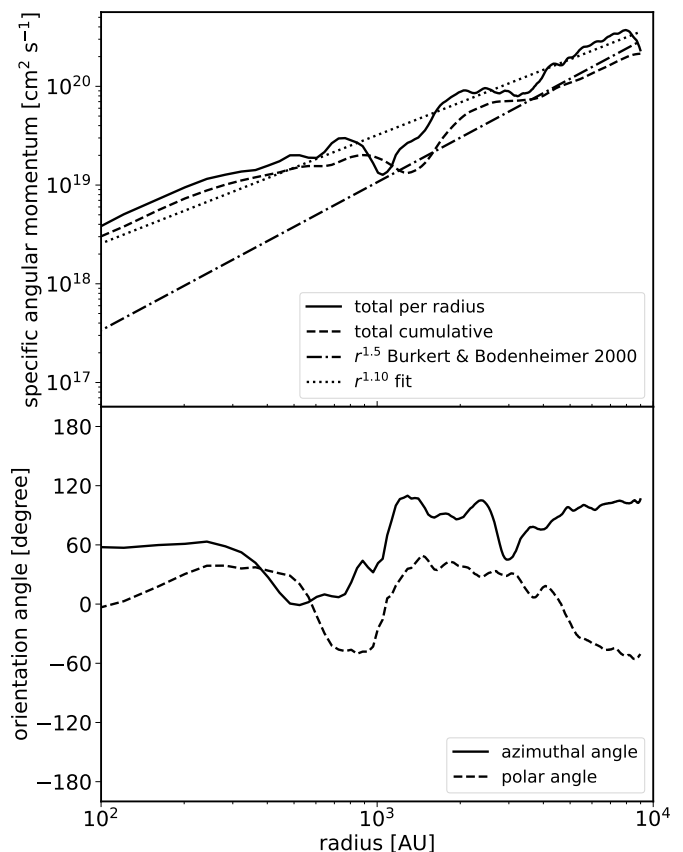


Fig. 3: Total specific angular momentum of the forming core and its orientation 93.2 kyr before collapse. The upper panel shows the angular momentum of each radial shell as solid line as well as the cumulative total angular momentum up to that radius as dashed lines. We fit a slope to the former which shows that they both follow a close to linear trend given by the dotted line. We also plot the predicted slope for turbulent cores by Burkert & Bodenheimer (2000) as the dashed-dotted line. The lower panel shows the orientation of the total specific angular momentum vector of each radial shell.

the dashed line as well as the turbulent Bonnor-Ebert profile where we take into account the support of a turbulent pressure component to the sound speed as

$$\sigma_{\text{tot}} = \sqrt{c_s^2 + \sigma_{1D}^2} \quad (2)$$

where $\sigma_{1D} = \sigma_{3D}/\sqrt{3}$ is the turbulent velocity in one dimension which we calculate from the mean of the three-dimensional turbulent velocity of radial bins around the density maximum. This velocity is shown as solid line in the bottom panel of Figure 2. One can see that the turbulent velocity is relatively constant throughout the Bonnor-Ebert sphere at a value with a mean of 0.096 km s^{-1} which we use for our turbulent Bonnor-Ebert profile in the upper panel given by the dotted line. The actual density seems to match the turbulent profile better, the error bars however are too large to distinguish between the isothermal and turbulent profile.

We also check if there is an overall rotation of the core which provides the angular momentum for the formation of a disk and which can potentially influence the formation of streamers. For a core with solid body rotation there are analytic models which predict the accretion rate onto the disk as a function of time and

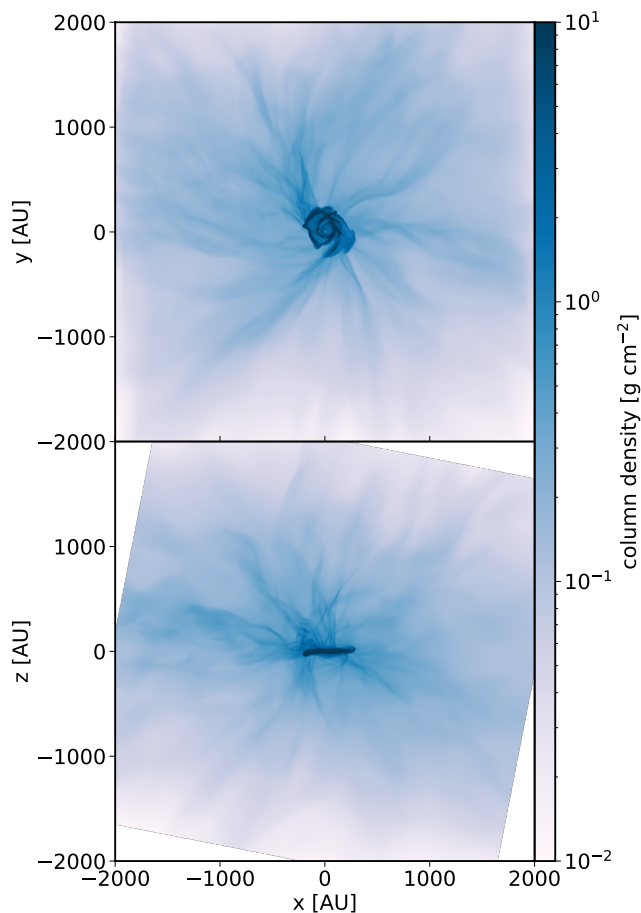


Fig. 4: Face-on and edge-on density projections of the forming disk at around 24.32 kyr after sink formation. The box has a size of 4000 AU around the central sink and is rotated to align the disk. The colour bar is adjusted to highlight the denser streamers flowing onto the disk. The density enhancements are accreted from all directions, as well as from above and below the disk, and extend to several thousand astronomical units.

radius (Ulrich 1976; Hueso & Guillot 2005). Therefore, we also plot the total specific angular momentum in the upper panel of Figure 3. We calculate the total specific angular momentum as

$$\mathbf{j}_{\text{tot}} = \frac{\sum \rho \mathbf{v} \times \mathbf{r}}{\sum \rho}, \quad (3)$$

where we use the density ρ , the velocity \mathbf{v} and the radial position \mathbf{r} of each cell. We determine the total specific angular momentum of each radial shell individually, shown as the solid line, as well as cumulatively for all cells within a given radius, shown by the dashed line. As the total angular momentum is non-zero, there is some bulk rotation which, however, is very small compared to overall turbulent motion.

Both curves, the one calculated per radius and the cumulative one, seem to scale close to linearly with the radius as indicated by the fit to the former value given by the dotted line with a slope of 1.10 ± 0.02 . This is due to the fact that the bulk velocity is relatively constant with radius, similar to the turbulent velocity. Observations of the cumulative total angular momentum rather suggest a scaling with radius to the power of 1.5 (Goodman et al. 1993; Caselli et al. 2002; Pirogov et al. 2003; Chen

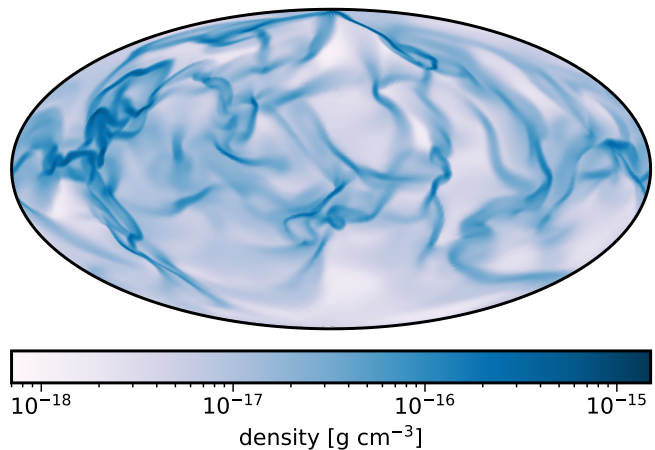


Fig. 5: Hammer projection of a spherical shell of the density at a distance of 400 AU from the central sink. The overdensities are visible as elongated density enhancements.

et al. 2007; Tobin et al. 2011; Yen et al. 2015). This scaling was proposed by Burkert & Bodenheimer (2000) as a consequence of sampling the turbulent velocity field at different scales and we also show it in the plot as dashed-dotted line. One can see, that it does not seem to match the total profiles as good as the linear fit. However, if we limit the fitted area to typical scales used in observations of above 1000 AU, the slope is slightly steeper with a slope of 1.21 ± 0.02 which matches both scalings similarly well.

While there seems to be some bulk rotation, the core shows no signs of solid body rotation which would suggest the total angular momentum to be proportional to the radius squared. Moreover, the bulk motion is not necessarily rotating in the same direction throughout the core as shown by the lower panel. Here, we plot the direction of the angular momentum vector for each radial shell. As one can see the azimuthal and polar angle are constantly changing throughout the core which proves that there is no ordered overall rotation.

After a short time, the core begins to collapse and a sink particle forms in its centre. Over time, more and more material falls onto the sink particle and, as not all of it is accreted directly, a disk forms around it. This situation is shown in Figure 4 which shows a face and edge-on projection of the density within a box of 4000 AU centred around the central sink particle. The sink has reached a mass of $0.68 M_{\odot}$ and the disk a mass of $0.09 M_{\odot}$ at 24.32 kyr after the sink formation. Depending on the column density contrast, one can clearly make out denser streams of material of lengths of up to several thousand AU flowing onto the disk. They do not necessarily settle to the disk plane before hitting the disk, but also seem to be accreted within the disk. For the further analysis of the streamer properties, we will concentrate on this snapshot.

In order to investigate the geometry of the streamers, we cut a spherical shell out of the three-dimensional density distribution at a radius of 400 AU from the central sink particle and project it on a map using a Hammer projection as shown in Figure 5. One can see, that most of the area is filled by low density material of around $1.0 \times 10^{-18} \text{ g cm}^{-3}$ and that the denser material of more than $1.0 \times 10^{-16} \text{ g cm}^{-3}$ forms concentrated, distinct structures. If the streamers would be filamentary by nature, they would appear as point-like density enhancements where they cross the shell. However, most of the higher density structures show a large ex-

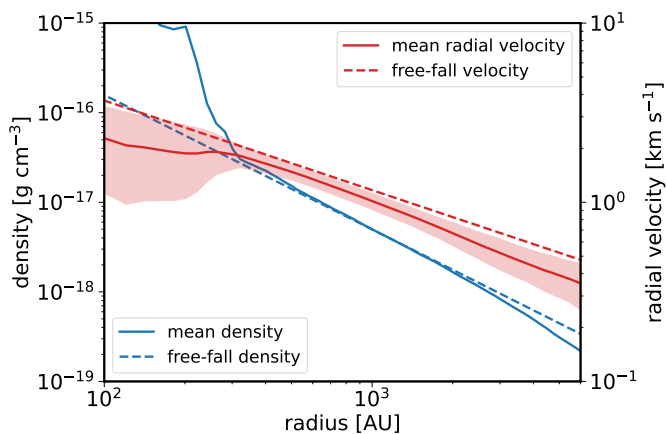


Fig. 6: Radially averaged density and velocity profiles during collapse. The mean density is given by the solid blue and the mean radial velocity by the solid red line. We also show the expected density and velocity profile assuming a free-fall model given by the blue and red dashed lines, respectively.

ment in one direction which is typical of sheet-like structures. This also becomes apparent when looking at the density projection around the disk in different angles which show vastly different configurations of density enhancements which is caused by the projection of sheets along the line-of-sight. The sheet-like geometry of the overdensities was already noted in Kuffmeier et al. (2017) and is consistent to large radii, however the density contrast also becomes weaker which can be seen below in Figure 12 where we show the density maps for larger distances. We also note, that the Hammer projections are created from an interpolation on a grid of regular angle spacing. However, the statistical analysis shown in the next sections is performed on a Healpix map (Gorski et al. 1999) which uses an equal-area and iso-latitude pixelisation in order to circumvent an oversampling of high latitudes.

3.2. Infall velocities and accretion

In order to measure the infall, we calculate the mean density and mean radial velocity at every radius which we show in Figure 6 as the solid blue and red line together with the standard deviation of the radial velocity shown as the shaded red area. The standard deviation of the density is quite large, especially for small radii as the density varies over three orders of magnitude. Therefore, we do not show it in order to keep the plot legible. We compare the resulting profiles to the expected density and velocity of free-fall collapse given by the dashed blue and red line, respectively. The free-fall velocity is given by

$$v_{\text{ff}} = \sqrt{\frac{2G(M_* + M_{\text{disk}})}{r}}, \quad (4)$$

with M_* and M_{disk} being the mass of the central sink particle and the disk and r being the radius. The free-fall density is then calculated assuming that the mass accretion rate

$$\dot{M} = 4\pi r^2 \rho v_{\text{ff}} \quad (5)$$

is constant, at least for small radii, as there is no mass build-up in a radial shell. We also observe that the mass accretion rate is roughly constant at around $2.6 \times 10^{-5} M_{\odot} \text{yr}^{-1}$ which we use to

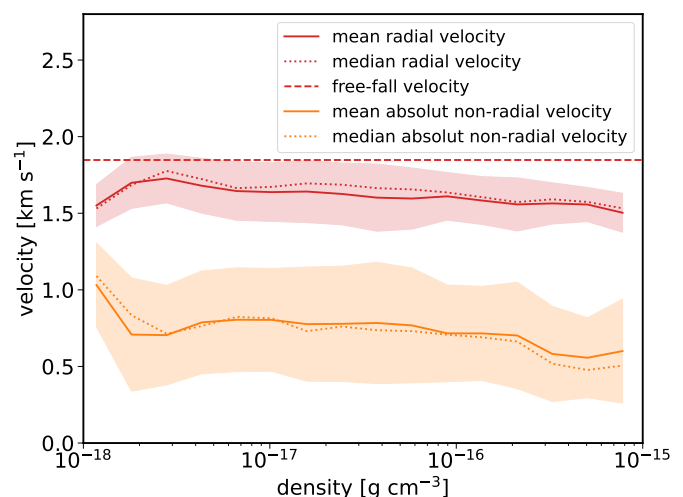


Fig. 7: Velocity statistics as function of density at a distance of 400 AU. The mean radial velocity is shown by the solid red and the mean absolute non-radial velocity by the solid orange line together with their standard deviation given by their respective shaded area. In addition, we also plot the median velocities given by the dotted lines and the free-fall velocity for the given central mass and distance shown by the dashed line.

derive the density profile of

$$\rho_{\text{ff}} = \frac{\dot{M}}{4\pi\sqrt{2GM_*}r^3}. \quad (6)$$

One can see that both, the density and velocity, follow closely the free-fall model. For small radii below 280 AU, the density shows a strong increase which is the accretion shock onto the outer radius of the disk where the infall velocity also reaches a maximum. For larger radii above 3000 AU, we see that the free-fall model is not a good description of the infall anymore which is where pressure effects start to play a larger role and where we have a transition to the filament material.

An interesting aspect of the collapse is whether the density enhancements have a different radial and angular velocity compared to the low density regions. As material is concentrated into denser structures, its angular momentum could add up and force it onto more non-radial dominated orbits or the angular momentum could cancel out, forcing it onto more radial orbits. However, there does not seem to be a strong trend which we show in Figure 7. At a distance of 400 AU, we calculate the mean radial and absolute angular velocity within sixteen different logarithmic density bins, given by the solid red and orange line, respectively. In addition, we also calculate the median value as the distribution of the velocity within each density bin is not necessary Gaussian. As one can see the radial velocity is relatively independent of the density, despite it spanning three orders of magnitude. Overall, it is slightly lower but very close to the free-fall velocity given by the dashed red line of about 1.8 km s^{-1} . The offset could be due to the reason that the disk at this distance cannot be approximated as a point-like gravitational source which should lead to a slightly lower free-fall velocity at small radii. There is a small decrease of the mean radial velocity in the very low density bin and a very shallow trend to lower velocities at the very high density bins. The reason for this at very low densities could be that the material can be more easily diverted onto non-radial orbits due to the gravitational attraction of the denser

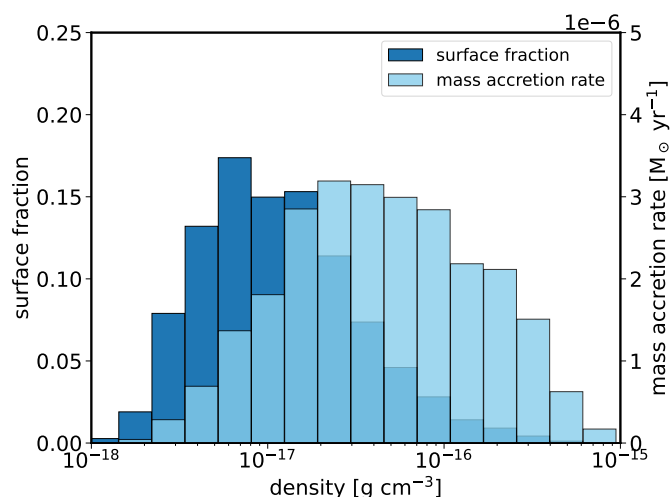


Fig. 8: Mass accretion distribution as function of density at a distance of 400 AU from the central sink particle. The dark blue bars show the distribution of the surface fraction of each density bin and the light blue bars show their respective total accretion rate. As one can see, most mass is accreted at high densities and low surface fractions.

gas. We investigate this by looking at the mean absolute non-radial velocity component given in each density bin by the orange solid line in Figure 7 with a standard deviation depicted by the orange shaded area. The non-radial motions are much slower than the radial collapse with values of around 0.75 km s^{-1} . And indeed, the lowest density bin shows a slight increase in non-radial motions indicating that there is a process forcing material onto non-radial orbits. We also see a general trend to slower velocities for larger densities which could be caused by the collimation of material into sheets where there is some canceling of angular momentum.

A consequence of a relatively uniform infall velocity is that the mass accretion rate scales with the density. This means that most of the mass which lands in the disk is accreted via the denser structures. We visualise this fact in Figure 8 where we plot the surface fraction in dark blue and the mass accretion rate in light blue in the same density bins as in Figure 7. While most cells show a low density, with the maximum being at around $6.0 \times 10^{-18} \text{ g cm}^{-3}$, it is the high density cells above $2.0 \times 10^{-17} \text{ g cm}^{-3}$ where most mass is accreted. Focussing only on the very dense structure above $1.0 \times 10^{-16} \text{ g cm}^{-3}$ shows that close to half of the total mass accretion rate through the shell, namely $1.24 \times 10^{-5} \text{ M}_{\odot} \text{ Myr}^{-1}$ of $2.58 \times 10^{-5} \text{ M}_{\odot} \text{ Myr}^{-1}$, is accreted in only a fraction of 0.1 of the total surface. Therefore, the dense accretion structures play an essential role in bringing in material to small scales. Moreover, given that Figure 7 shows that the angular velocity and thus the specific angular momentum is relatively constant in each density bin. Therefore, the accretion of absolute angular momentum shows the same distribution as the mass accretion rate.

Additionally, it is vital to understand where the material enters the disk as not all material is accreted at the outer radius. We measure the mass accretion rate onto the disk at each radius by azimuthally summing up the flux through the surfaces located 10 cells above and below the central plane using the velocity perpendicular to the disk. We show the resulting total mass accretion rate in Figure 9 as the black solid line together with its side of origin, either the top or bottom face, as red and teal dashed lines.

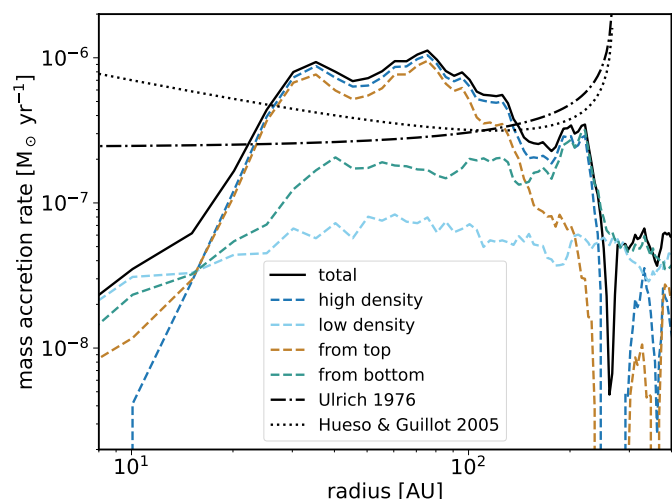


Fig. 9: Total mass accretion onto the disk measured at 10 cells above and below the central plane given by the solid black line together with predictions from solid body rotation shown as dashed-dotted and dotted black lines. Compared to the models, we measure an increased mass accretion rate at intermediate radii. The total mass accretion rate is split into its side of origin as shown by the red and teal dashed lines and its density given by the light and dark blue dashed lines.

We also split the total mass accretion rate into low and high density material with a threshold density of $1.0 \times 10^{-16} \text{ g cm}^{-3}$ and plot the corresponding rates as light and dark blue dashed lines. As one can see, most mass is accreted between 30 and 100 AU with a steep drop towards smaller and larger radii up to the maximum extent of the disk of about 280 AU. The integral over all radii equals the total mass accretion rate of $2.58 \times 10^{-5} \text{ M}_{\odot} \text{ Myr}^{-1}$ which we already measured on larger scales. While this only represents one measurement for this particular point in time, we do observe this pattern of accretion onto intermediate radii to be relatively stable over timescales of several ten thousand years when normalising for the disk size.

The accretion itself is highly asymmetrical which can be seen in the separate accretion rates for the different sides of the disk. While it is dominated at large radii by accretion coming from below the disk, the accretion at lower radii is mainly coming from above. This can also be observed in the projection plots of Figure 4 and implies that the angular momentum is not distributed isotropically. Looking at the split-up between low and high density, one can also see that the bulk of the mass accretion consists of high density material. This could already be seen from Figure 8, but shows that the density enhancements continue down onto the disk itself. Interestingly, the low density regime does not display the same strong tendency for a preferred accretion radius but shows a more distributed, albeit negligible, accretion with a similar rate at all radii.

We also include predictions from two different models for the mass accretion rate of a core under solid body rotation. Although we already showed that the initial core does not rotate as a solid body, this is the only model for which an analytic description of the mass accretion rate exist. The dashed-dotted line shows the model by Ulrich (1976) which assumes that every mass element of a radial shell hits the disk under a parabolic orbit according to its angular momentum with the central sink being in its focus. This leads to the so-called source function, the mass accretion

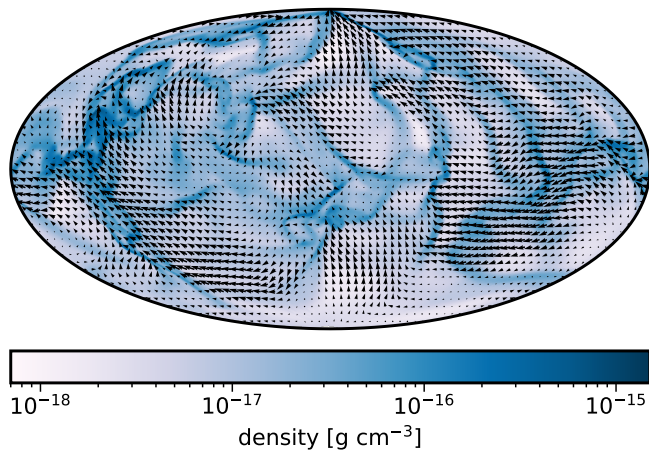


Fig. 10: The same Hammer projection of the density given in Figure 5 together with respective velocity vectors indicating the direction and magnitude of the motions perpendicular to the infall.

rate per azimuthal surface:

$$S_U(r, t) = \frac{\dot{M}(t)}{4\pi r_c(t)^2} \left(\frac{r}{r_c(t)} \right)^{-1} \left(1 - \frac{r}{r_c(t)} \right)^{-1/2} \quad (7)$$

with r_c being the centrifugal radius, the maximum impact radius, given by

$$r_c = \frac{\Omega^2 r_0^4}{GM_*} \quad (8)$$

which depends on the shells angular speed Ω and its radius r_0 . The dotted line uses the model by Hueso & Guillot (2005) which assumes that the material is accreted directly onto its respective Keplerian radius leading to a slightly more centrally dominated source function:

$$S_H(r, t) = \frac{\dot{M}(t)}{8\pi r_c(t)^2} \left(\frac{r}{r_c(t)} \right)^{-3/2} \left(1 - \sqrt{\frac{r}{r_c(t)}} \right)^{-1/2}. \quad (9)$$

In principle, the mass accretion rate and the centrifugal radius both depend on time. However, in the case of free-fall, the mass accretion rate is constant and the evolution of centrifugal radius can be described analytically. In our case, where we do not start with solid body rotation, we cannot calculate the centrifugal radius as function of time. Therefore, we use the radial extent of the disk of 280 AU as an estimate for the models. As expected, the measured mass accretion rate deviates strongly from the solid body rotation case which predicts larger accretion rates towards the centre and close to the centrifugal radius. The deficit of material coming in at small radii is a consequence of the accreted material lacking very low angular momentum. For solid body rotation this is the material close to the rotational axis. However, due to the turbulent initial condition, there is no ordered rotation and therefore not much gas with very low angular momentum. The same argument is valid inversely for the mass accretion rate at very large radii. For solid body rotation this is given by the material in the plane of rotation. However, in our case, the maximum angular momentum is limited by the random motion of the gas which is statistically more unlikely to reach large values consistently.

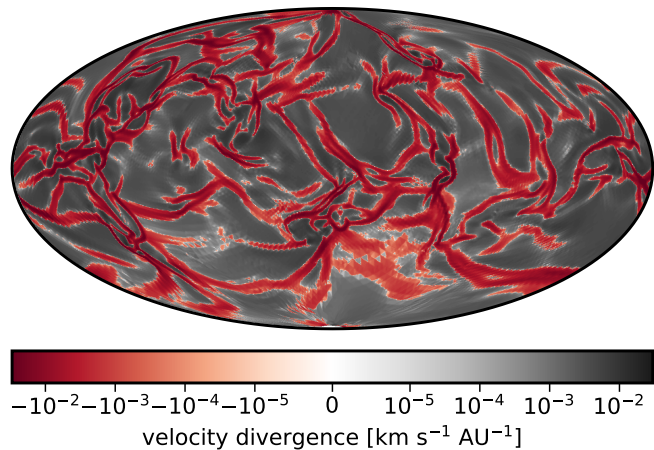


Fig. 11: Hammer projection of the velocity divergence of the non-radial velocity components at 400 AU distance from the central sink particle. Areas in red show structures where material is compressed due to the velocity field.

As the core is collapsing essentially in free-fall and each shell is accreted consecutively with larger and larger angular momentum, the mean main accretion radius should be set by the total angular momentum of the shell where the gas originated. As not all mass of the shell is combined into one accretion stream, there should be some spread in angular momentum of the individual overdensities. However, this spread should be around the total angular momentum of the original shell. We can test this by determining the original radius in two different ways. On the one hand, we can compare the angular momentum of the current mean main accretion to the initial angular momentum distribution. On the other hand, we can calculate the distance the current main accretion travelled under the assumption of free-fall collapse.

To estimate the total angular momentum we use the mass accretion peak at 80 AU and the angular velocity of the dense gas of around 0.6 km s^{-1} to get a rough value of $7.0 \times 10^{19} \text{ cm}^2 \text{ s}^{-1}$. Comparing this value to Figure 3 this means that the material is coming from a shell of roughly two to three thousand AU. The distance the gas would travel due to the free-fall time in about 25 kyr also equals around two thousand AU. This means that here the main accretion radius indeed seems to be set by the shell's angular momentum. If the angular momentum of accretion streams is always distributed around the shells original total angular momentum, the mean main accretion radius should expand over time as its value is increasing with further distance. However, because the angular momentum of each individual shell is not always aligned to the other shells, accretion is also able to heavily disrupt the disk. We also observe this in our simulation where the disk size can change quite drastically over time.

3.3. Residual velocities

From the analysis of the radial velocity it is clear that essentially all material is falling onto the central sink in a free-fall manner. This only leaves the residual motions perpendicular to the infall as cause of the collimation of material into denser sheets. Therefore, we analyse the residual velocities in more detail. In Figure 10, we show the same map as in Figure 5 with the perpendicular motions displayed on top where we use the azimuthal and

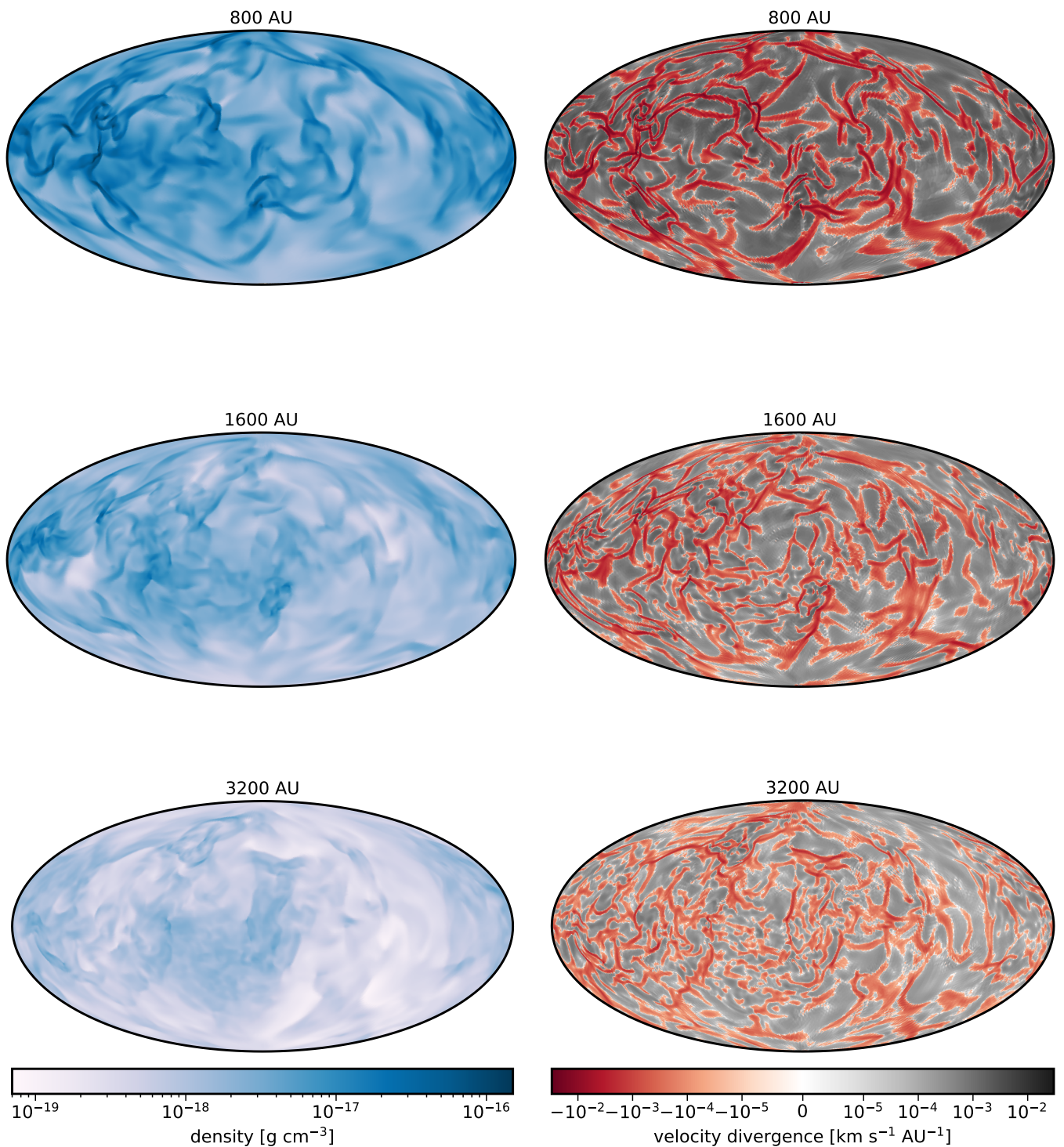


Fig. 12: Hammer projections of the density and velocity divergence at different distances for the same time step. From top to bottom we show further and further radii. As one can see, during infall the gas forms less but more condensed structures the closer it gets to the central sink particle.

polar velocity components to determine the direction and magnitude of the flow. As one can see, the density enhancements coincide either with strong changes in magnitude of the flow or where two flows converge. This means that the main locations of the formation of accretion sheets are given by where gas with

different angular momentum collides and forms shock-like density enhancements.

In order to emphasise this point, we also calculate the velocity divergence of the residual motions which we show in Figure 11. Note that this map only takes into consideration the azimuthal and polar velocities and neglects the radial velocity com-

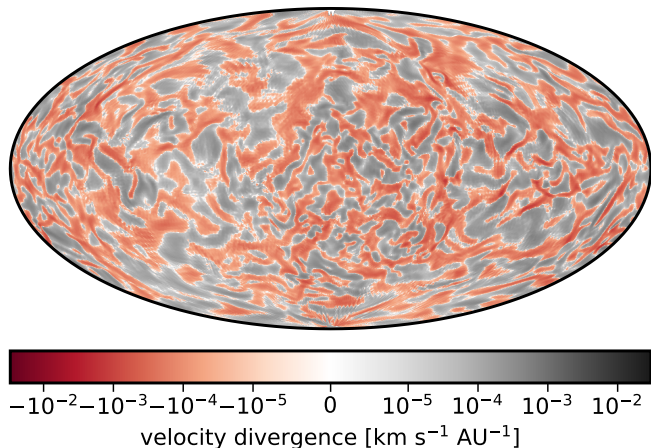


Fig. 13: Velocity divergence at 3200 AU at around 93.2 kyr before sink formation. The velocity field is dominated by turbulent motions and already shows the typical structures visible during collapse in Figure 12 which lead to the formation of the dense accretion sheets.

ponent. Negative values of the velocity divergence shown in red are areas where material is being compressed and positive values in gray show areas where material is being diluted. Comparing the map to the density map of Figure 10, one can clearly see that the areas of compression coincide with overdensities which shows again that it is the flows of the residual motions during free-fall which bring material together into denser accretion sheets.

During infall, there will be a wide range of angular momentum. Gas with more eccentric orbits will at some point cross the orbits of the more radially dominated orbits of the denser accretion sheets. This means the density enhancements will accumulate more and more material along their way, leading to fewer but even denser structures. We show this effect in Figure 12. From top to bottom we plot the density and velocity divergence at further and further distances. As one can see, as the size and contrast of structures visible in the density goes down the farther out we go, the residual motions define more and more small scale convergence zones. Even at large distances, where radial collapse has not yet collimated a lot of material and the residual motions are still dominated by the turbulent velocity field of the filament, one can already observe convergence zones. This suggests that the initial seeds of overdensities are given by the turbulent motions on large scale. In order to verify that it is the turbulent velocity field which creates this pattern, we also plot the velocity divergence around the core of Figure 1 at 93.2 kyr before the collapse in Figure 13. Here, the forming core only consists of an overdensity of a factor of two. As one can see, even at this early stage where there is no radial collapse yet, a very similar pattern is visible. This means that the initial turbulence on large scales indeed sets the formation pattern of the dense accretion sheets.

One can also measure the collimation of material during infall in the density probability distribution at different distances as shown in Figure 14. From light to dark blue, we plot the density probability distribution of spherical shells starting from large distances down to close to the disk. One can see a systematic trend where the density at large distances follows a log-normal distribution with a dispersion of $\sigma = 0.62 \pm 0.02$, whereas if one goes closer to the disk, one can see the development of a power-

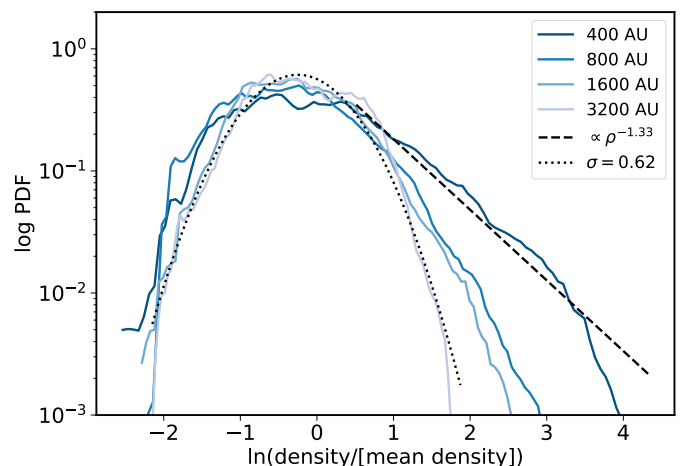


Fig. 14: Density probability distribution of shells at different distances as given by the legend. The distribution follows a log-normal function with gas closer to the central sink particle showing the development of a power-law.

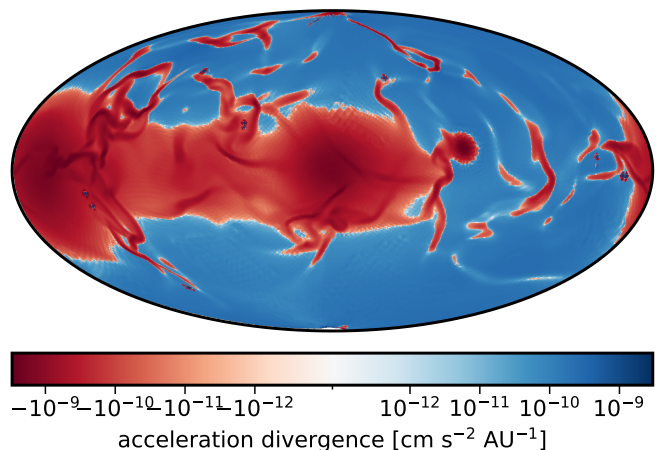


Fig. 15: Hammer projection of the acceleration divergence at 400 AU from the central sink particle. Negative values show areas where material is gravitationally compressed and positive values where it is pulled apart. The gravitational compression of the disk is visible as the large distributed area together with the most massive accretion structures.

law tail. In that regard, the evolution from larger to smaller radii follows a similar process as the density in a turbulent box under gravitational collapse. The longer gravity is able to compress the material, the more pronounced the power-law tail becomes. This suggests the same process is happening during the infall onto the central sink. Indeed, if we fit a power-law to the high-density tail we get a similar but slightly smaller index of -1.33 ± 0.03 as in simulations of turbulent boxes which vary around -1.5 up to -2.5 (Kritsuk et al. 2011; Federrath & Klessen 2013). This suggests that gravity plays an essential role for the evolution of the overdensities which we will explore in the following subsection.

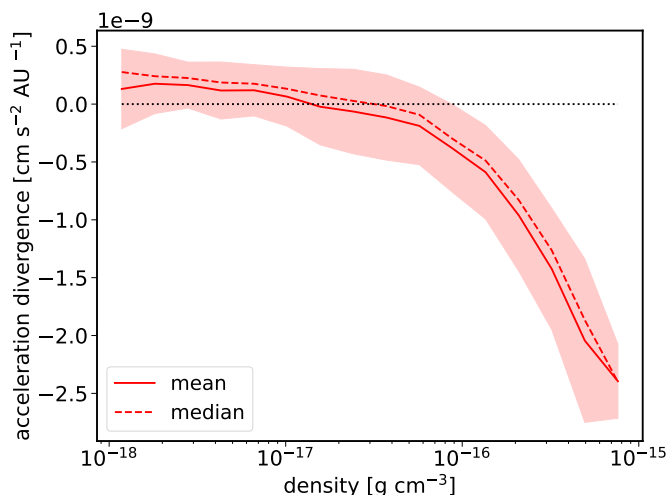


Fig. 16: Mean acceleration divergence per density bin at 400 AU distance of the central sink together with its standard deviation. While for low densities the divergence is positive and small, one can see that the gravitational compression dominates for densities larger than $1.0 \times 10^{-16} \text{ g cm}^{-3}$ where there is a steep drop to large negative values.

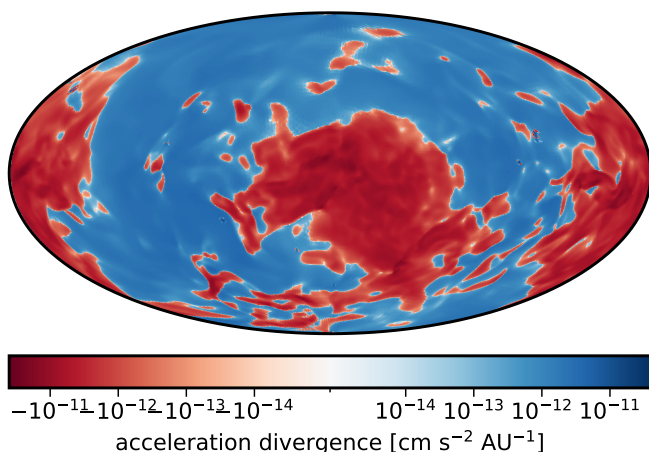


Fig. 17: Hammer projection of the acceleration divergence at 3200 AU from the central sink particle. The centre and the border of the image point in the direction of the filament. The plot shows the large-scale gravitational acceleration onto the central axis due to the filament potential.

3.4. Are the overdensities gravitationally dominated?

In order to explore the question if the overdensities gravitationally dominate their local environment, we calculate the divergence of the acceleration field analogously to the velocity field and show the results in Figure 15. Negative values coloured in red show areas where material is gravitationally compressed while positive values coloured in blue show areas where material is being gravitationally pulled apart. Very prominent is the gravitational attraction of the disk itself, pulling material into the central plane. It dominates over the gravitational pull of the streamers except for the area towards the right hand side of the viewing direction. Here it is interrupted by the gravitational field of one of the densest streamers and a close-by sink particle which

pull the gas stronger into their direction, turning their vicinity blue. Compared to Figure 5, one can see that there is a one-to-one correspondence of the highest overdensities to areas with large negative divergence of the acceleration. However, not all structures are able to gravitationally pull material together. Some overdensities visible in the density map have no correspondence in the acceleration divergence map. We investigate this further in Figure 16 where we show the mean and median acceleration divergence as function of the density using the same bins as in Figure 7. As one can see, only the very dense structures above around $1.0 \times 10^{-16} \text{ g cm}^{-3}$ show a significant negative acceleration divergence which means only the densest fraction of the overdensities are able to gravitationally concentrate material at this radius.

This pattern remains the same going to larger distances until the gravitational pull onto the central axis of the filament dominates as can be seen in Figure 17. Compared, to the small scale velocity divergence at large distances visible in Figure 12, the missing gravitational divergence of small scale structure means that overdensities are mainly initialised by the velocity field. During infall, they are collimated and accrete enough material to gravitationally dominate their vicinity and gather even more material. This explains the increase in non-radial orbits of low density material which can be easily pulled towards the dense streamers seen in Figure 7 as well as the development of a power-law tail in the density probability function observed in Figure 14.

4. Comparison to related work

Our main finding that the accretion is set by the large-scale environment agrees with other simulations such as Kuffmeier et al. (2017), Bate (2018) and Lebreuilly et al. (2021). We show that the formation of overdensities occurs naturally in a turbulent environment due to the initial velocity field. We find that this has a strong influence on where mass is accreted onto the disk. However, this effect may depend strongly on the included physics. For example, the simulation of Lee et al. (2021) which includes magnetic fields finds a centrally concentrated mass accretion.

Although the general outcome of overdensity formation during collapse is robust for different initial conditions, we made several simplifications in our simulations. We conducted this work in order to set a baseline to compare future parameter studies to. Of major importance would be the inclusion of magnetic fields. Depending on the strength of the magnetic field, it can have a significant impact on the gas dynamics, potentially leading to a reduction of overdensities. Magnetic fields also have a strong effect particularly on the sizes of disks due to magnetic braking and outflows (Allen et al. 2003; Galli et al. 2006; Price & Bate 2007; Hennebelle & Fromang 2008; Duffin & Pudritz 2009; Commerçon et al. 2010; Seifried et al. 2011, 2012b) which typically leads to rather small disk radii. While we deliberately did not analyse the disk properties in this study, we do find a rather large disk. However, it is still in a very dynamic stage where the size can vary quite drastically. Moreover, depending on dust properties and cosmic-ray ionisation rates, non-ideal MHD effects can reduce the impact of strong magnetic fields, which again leads to more frequent disk formation and larger disk sizes (Shu et al. 2006; Tsukamoto et al. 2015a; Masson et al. 2016; Zhao et al. 2016, 2018; Wurster & Bate 2019). Furthermore, there is also evidence that the effect of magnetic braking can be reduced by non-idealised initial conditions where turbulence plays an essential role, not necessarily for magnetic reconnection, but by misaligning the angular momentum from the magnetic field vector (Hennebelle & Ciardi 2009; Seifried et al.

2012a, 2013; Joos et al. 2013; Li et al. 2013; Wurster et al. 2019; Hirano et al. 2020). A comparison of the accretion including MHD effects will be the focus of a future study.

In addition, while many studies include a barotropic equation-of-state in order to mimic thermal effects of the disk above the opacity limit, radiative feedback from the star has been shown to affect the temperature structure and therefore the fragmentation of the disk (Commerçon et al. 2010; Tsukamoto et al. 2015b). Moreover, thermal pressure is able of driving outflows even in the complete absence of magnetic fields (Bate 2011; Bate et al. 2014). To which extent radiative feedback has an effect on overdensities in the accretion flow has to be explored in future simulations

5. Conclusions

In this study, we simulated the collapse of a core which forms self-consistently within a turbulent filament in order to analyse the origin and properties of overdensities in the accretion flow. We analysed the morphological, kinematic and gravitational properties of the core before and during the collapse in great detail and are able to draw the following conclusions:

1. Overdensities in the accretion flow are created naturally as a consequence of the initial turbulent velocity field. This velocity field is set on large scales and is already present before the collapse.
2. Instead of having a filamentary morphology, we find that the overdensities in our simulation are rather sheet-like where the observable accretion pattern depends on the line-of-sight projection. This morphology follows from the shock-like convergence of residual motions during collapse.
3. The collapse is essentially in free-fall with no significant difference in the radial velocity of the high and low-density gas despite it spanning several orders of magnitude. We only see a slight tendency for lower angular velocities, e.g. more direct radial infall, of the high density gas and higher angular velocity, e.g. more eccentric infall, of the low density gas.
4. The mass accretion onto the disk differs drastically from an idealised initial condition of a core with solid body rotation. This is due to the fact that the core inherits a turbulent velocity distribution from its environment with no generally ordered rotation.
5. The turbulent velocity field defines a log-normal probability density function at large radii which develops a power-law tail at smaller radii, similar to the gravitational collapse in a turbulent box.
6. Both, the increase in angular velocity at low densities and the development of a power-law tail at large densities, are a consequence of the gravitational pull of the most massive overdensities which are able to gravitationally dominate their local environment. This leads to more and more collimated structures over time during the infall.

Acknowledgements. This research was supported by the Excellence Cluster ORIGINS which is funded by the Deutsche Forschungsgemeinschaft (DFG, German Research Foundation) under Germany's Excellence Strategy - EXC-2094 - 390783311.

References

Allen, A., Li, Z.-Y., & Shu, F. H. 2003, *ApJ*, 599, 363
 André, P., Di Francesco, J., Ward-Thompson, D., et al. 2014, in *Protostars and Planets VI*, ed. H. Beuther, R. S. Klessen, C. P. Dullemond, & T. Henning, 27–51

Ansdell, M., Williams, J. P., Manara, C. F., et al. 2017, *AJ*, 153, 240
 Bae, J., Hartmann, L., & Zhu, Z. 2015, *ApJ*, 805, 15
 Bate, M. R. 2011, *MNRAS*, 417, 2036
 Bate, M. R. 2018, *MNRAS*, 475, 5618
 Bate, M. R., Tricco, T. S., & Price, D. J. 2014, *MNRAS*, 437, 77
 Burkert, A. & Bodenheimer, P. 2000, *ApJ*, 543, 822
 Cabedo, V., Maury, A., Girart, J. M., & Padovani, M. 2021, *A&A*, 653, A166
 Caselli, P., Benson, P. J., Myers, P. C., & Tafalla, M. 2002, *ApJ*, 572, 238
 Chen, X., Launhardt, R., & Henning, T. 2007, *ApJ*, 669, 1058
 Commerçon, B., Hennebelle, P., Audit, E., Chabrier, G., & Teyssier, R. 2010, *A&A*, 510, L3
 Drażkowska, J. & Dullemond, C. P. 2018, *A&A*, 614, A62
 Duffin, D. F. & Pudritz, R. E. 2009, *ApJ*, 706, L46
 Federrath, C. & Klessen, R. S. 2013, *ApJ*, 763, 51
 Foster, P. N. & Chevalier, R. A. 1993, *ApJ*, 416, 303
 Galli, D., Lizano, S., Shu, F. H., & Allen, A. 2006, *ApJ*, 647, 374
 Goodman, A. A., Benson, P. J., Fuller, G. A., & Myers, P. C. 1993, *ApJ*, 406, 528
 Gorski, K. M., Wandelt, B. D., Hansen, F. K., Hivon, E., & Banday, A. J. 1999, *arXiv e-prints, astro*
 Greaves, J. S. & Rice, W. K. M. 2011, *MNRAS*, 412, L88
 Harsono, D., Bjerkeli, P., van der Wiel, M. H. D., et al. 2018, *Nature Astronomy*, 2, 646
 Heigl, S., Burkert, A., & Gritschneider, M. 2018, *MNRAS*, 474, 4881
 Heigl, S., Gritschneider, M., & Burkert, A. 2020, *MNRAS*, 495, 758
 Hennebelle, P. & Ciardi, A. 2009, *A&A*, 506, L29
 Hennebelle, P., Commerçon, B., Lee, Y.-N., & Charnoz, S. 2020, *A&A*, 635, A67
 Hennebelle, P. & Fromang, S. 2008, *A&A*, 477, 9
 Hirano, S., Tsukamoto, Y., Basu, S., & Machida, M. N. 2020, *ApJ*, 898, 118
 Hsieh, T.-H., Hirano, N., Belloche, A., et al. 2019, *ApJ*, 871, 100
 Hsieh, T. H., Segura-Cox, D. M., Pineda, J. E., et al. 2023, *A&A*, 669, A137
 Hueso, R. & Guillot, T. 2005, *A&A*, 442, 703
 Joos, M., Hennebelle, P., Ciardi, A., & Fromang, S. 2013, *A&A*, 554, A17
 Kido, M., Takakuwa, S., Saigo, K., et al. 2023, *ApJ*, 953, 190
 Kritsuk, A. G., Norman, M. L., & Wagner, R. 2011, *ApJ*, 727, L20
 Kruijter, T. S., Burkhardt, C., Budde, G., & Kleine, T. 2017, *Proceedings of the National Academy of Science*, 114, 6712
 Kruijter, T. S., Touboul, M., Fischer-Gödde, M., et al. 2014, *Science*, 344, 1150
 Kuffmeier, M., Calcutt, H., & Kristensen, L. E. 2019, *A&A*, 628, A112
 Kuffmeier, M., Dullemond, C. P., Reissl, S., & Goicovic, F. G. 2021, *A&A*, 656, A161
 Kuffmeier, M., Frimann, S., Jensen, S. S., & Haugbølle, T. 2018, *MNRAS*, 475, 2642
 Kuffmeier, M., Haugbølle, T., & Nordlund, Å. 2017, *ApJ*, 846, 7
 Kuffmeier, M., Jensen, S. S., & Haugbølle, T. 2023, *European Physical Journal Plus*, 138, 272
 Kuznetsova, A., Bae, J., Hartmann, L., & Mac Low, M.-M. 2022, *ApJ*, 928, 92
 Kwon, W., Looney, L. W., Mundy, L. G., Chiang, H.-F., & Kamball, A. J. 2009, *ApJ*, 696, 841
 Lam, K. H., Li, Z.-Y., Chen, C.-Y., Tomida, K., & Zhao, B. 2019, *MNRAS*, 489, 5326
 Larson, R. B. 1969, *MNRAS*, 145, 271
 Le Gouellec, V. J. M., Hull, C. L. H., Maury, A. J., et al. 2019, *ApJ*, 885, 106
 Lebreuilly, U., Hennebelle, P., Colman, T., et al. 2021, *ApJ*, 917, L10
 Lee, Y.-N., Charnoz, S., & Hennebelle, P. 2021, *A&A*, 648, A101
 Lesur, G., Ercolano, B., Flock, M., et al. 2022, *arXiv e-prints, arXiv:2203.09821*
 Lesur, G., Hennebelle, P., & Fromang, S. 2015, *A&A*, 582, L9
 Li, Z.-Y., Krasnopolsky, R., & Shang, H. 2013, *ApJ*, 774, 82
 Manara, C. F., Morbidelli, A., & Guillot, T. 2018, *A&A*, 618, L3
 Masson, J., Chabrier, G., Hennebelle, P., Vaytet, N., & Commerçon, B. 2016, *A&A*, 587, A32
 Matsumoto, T., Machida, M. N., & Inutsuka, S.-i. 2017, *ApJ*, 839, 69
 Morbidelli, A., Bitsch, B., Crida, A., et al. 2016, *Icarus*, 267, 368
 Murillo, N. M., van Dishoeck, E. F., Hacar, A., Harsono, D., & Jørgensen, J. K. 2022, *A&A*, 658, A53
 Najita, J. R. & Kenyon, S. J. 2014, *MNRAS*, 445, 3315
 Pelkonen, V. M., Padoan, P., Haugbølle, T., & Nordlund, Å. 2021, *MNRAS*, 504, 1219
 Penston, M. V. 1969, *MNRAS*, 144, 425
 Pineda, J. E., Arzoumanian, D., Andre, P., et al. 2023, in *Astronomical Society of the Pacific Conference Series*, Vol. 534, *Protostars and Planets VII*, ed. S. Inutsuka, Y. Aikawa, T. Muto, K. Tomida, & M. Tamura, 233
 Pineda, J. E., Segura-Cox, D., Caselli, P., et al. 2020, *Nature Astronomy*, 4, 1158
 Pirogov, L., Zinchenko, I., Caselli, P., Johansson, L. E. B., & Myers, P. C. 2003, *A&A*, 405, 639
 Price, D. J. & Bate, M. R. 2007, *MNRAS*, 377, 77
 Segura-Cox, D. M., Schmiedeke, A., Pineda, J. E., et al. 2020, *Nature*, 586, 228
 Seifried, D., Banerjee, R., Klessen, R. S., Duffin, D., & Pudritz, R. E. 2011, *MNRAS*, 417, 1054

- Seifried, D., Banerjee, R., Pudritz, R. E., & Klessen, R. S. 2012a, MNRAS, 423, L40
- Seifried, D., Banerjee, R., Pudritz, R. E., & Klessen, R. S. 2013, MNRAS, 432, 3320
- Seifried, D., Banerjee, R., Pudritz, R. E., & Klessen, R. S. 2015, MNRAS, 446, 2776
- Seifried, D., Pudritz, R. E., Banerjee, R., Duffin, D., & Klessen, R. S. 2012b, MNRAS, 422, 347
- Shu, F. H. 1977, ApJ, 214, 488
- Shu, F. H., Galli, D., Lizano, S., & Cai, M. 2006, ApJ, 647, 382
- Testi, L., Birnstiel, T., Ricci, L., et al. 2014, in Protostars and Planets VI, ed. H. Beuther, R. S. Klessen, C. P. Dullemond, & T. Henning, 339–361
- Teyssier, R. 2002, A&A, 385, 337
- Thieme, T. J., Lai, S.-P., Lin, S.-J., et al. 2022, ApJ, 925, 32
- Tobin, J. J., Hartmann, L., Chiang, H.-F., et al. 2011, ApJ, 740, 45
- Tobin, J. J., Sheehan, P. D., Megeath, S. T., et al. 2020, ApJ, 890, 130
- Toro, E., Spruce, M., & Speares, W. 1994, Shock Waves, 4, 25
- Truelove, J. K., Klein, R. I., McKee, C. F., et al. 1997, ApJ, 489, L179
- Tsukamoto, Y., Iwasaki, K., Okuzumi, S., Machida, M. N., & Inutsuka, S. 2015a, MNRAS, 452, 278
- Tsukamoto, Y., Takahashi, S. Z., Machida, M. N., & Inutsuka, S. 2015b, MNRAS, 446, 1175
- Tychoniec, Ł., Manara, C. F., Rosotti, G. P., et al. 2020, A&A, 640, A19
- Tychoniec, Ł., Tobin, J. J., Karska, A., et al. 2018, ApJS, 238, 19
- Ulrich, R. K. 1976, ApJ, 210, 377
- Valdivia-Mena, M. T., Pineda, J. E., Segura-Cox, D. M., et al. 2022, A&A, 667, A12
- Valdivia-Mena, M. T., Pineda, J. E., Segura-Cox, D. M., et al. 2023, A&A, 677, A92
- Van Kooten, E. M. M. E., Wielandt, D., Schiller, M., et al. 2016, Proceedings of the National Academy of Science, 113, 2011
- van Leer, B. 1977, Journal of Computational Physics, 23, 276
- van Leer, B. 1979, Journal of Computational Physics, 32, 101
- Walch, S., Naab, T., Whitworth, A., Burkert, A., & Gritschneider, M. 2010, MNRAS, 402, 2253
- Wurster, J. & Bate, M. R. 2019, MNRAS, 486, 2587
- Wurster, J., Bate, M. R., & Price, D. J. 2019, MNRAS, 489, 1719
- Yen, H.-W., Koch, P. M., Takakuwa, S., et al. 2015, ApJ, 799, 193
- Zhao, B., Caselli, P., Li, Z.-Y., & Krasnopolsky, R. 2018, MNRAS, 473, 4868
- Zhao, B., Caselli, P., Li, Z.-Y., et al. 2016, MNRAS, 460, 2050